Received 31 March 2023; revised 25 April 2023; accepted 3 May 2023. Date of publication 9 May 2023; date of current version 19 May 2023.

Digital Object Identifier 10.1109/OJAP.2023.3274167

A 3D-Printed Encapsulated Dual Wide-Band Dielectric Resonator Antenna With Beam Switching Capability

REZA SHAMSAEE MALFAJANI [1] (Graduate Student Member, IEEE), HAMED NIKNAM [2], SAMPADA BODKHE [2], DANIEL THERRIAULT [2], JEAN-JACQUES LAURIN [1] (Senior Member, IEEE), AND MOHAMMAD S. SHARAWI [1] (Senior Member, IEEE)

[1] Department of Electrical Engineering, Polytechnique Montreal, Montreal, QC H3T 1J4, Canada

[2] Department of Mechanical Engineering, Polytechnique Montreal, Montreal, QC H3T 1J4, Canada

CORRESPONDING AUTHOR: R. SHAMSAEE MALFAJANI (e-mail: r.shamsaee@polymtl.ca)

This work was supported by the Fonds de recherche du Québec Nature et Technologies (FRQNT) under Grant 2022-PR-298793. The work of Hamed Niknam was supported by the de bourses de recherche du Québec Nature et technologies (FRQNT) Post-Doctoral Awards (B3X).

ABSTRACT This paper presents the concept of encapsulated dielectric resonator antennas (E-DRAs). In E-DRAs, smaller-sized DRAs with a specific permittivity is embedded inside a larger DRA with a lower permittivity allowing for simultaneous efficient radiation at two widely separated and widely covered frequency bands. In this work, the proposed E-DRAs cover both the sub-6-GHz band (with a large size DRA) and mm-wave band (with smaller sized DRAs) for 5G and beyond applications. The proposed design of the dual wide-band E-DRAs is fabricated using the fused filament fabrication (FFF) 3D printing process. At mm-wave bands, small cylindrical DRAs (cDRAs) are the radiating elements, and a larger cDRA in conjunction with a dielectric lens (DL) is used to achieve high gain radiation at such high bands. An array of 5 elements is used in a switched mode fashion to add switching beam capability to the antenna at the mm-wave band. Employing 3D printing reduces the fabrication time and cost and enables precise control of the dielectric constant of the DRAs. Measurement results show a maximum gain of 7.2 dBi at 3.2 GHz and 18 dBi at 31.5 GHz. The measured efficiency is more than 95% and 80% at sub-6-GHz and mm-wave bands, respectively. At the sub-6-GHz band, the measured 10-dB return loss bandwidth is 33% (centered at 3.6 GHz). At the mm-wave frequency band, the measured 10-dB return loss bandwidth is 27% (centered at 30.5 GHz). The achieved bandwidths are the highest among previous works on dual-band antennas at sub-6-GHz and mm-wave bands.

INDEX TERMS 3D printed antenna, 5G, beam steering, dielectric resonator antenna, dual-band, wideband antenna, additive manufacturing.

I. INTRODUCTION

THE RAPID development of wireless communication technology and applications has increased the demand for high-data-rate communication. This demand is addressed by using a wider bandwidth or operating at high frequencies. Two new wireless technologies that use this approach are 5G and beyond, and mobile satellite communication (SATCOM).

The challenges facing the design of antennas for 5G and beyond and mobile STACOM applications include the need for wide/multi-band operation, compact size, and high-gain to compensate for signal losses specifically at high frequencies. There is also a need for multi-band antennas to support existing low-frequency standards in addition to the new standards. In case of 5G, operation at both mm-wave and sub-6-GHz is desired to support for widely available 4G standard. These make the antenna design for the emerging communication technologies challenging due to the limited space available in mobile devices and the large size requirements at low frequencies (e.g., sub-6-GHz band) and the high material losses at high frequencies (e.g., mm-wave band).

Various types of dual-band antennas with high-frequency ratios and beam steering capability have been proposed with metallic structures. These antennas are low profile but exhibit narrow operating bandwidths and have low efficiencies due to the negative effect of surface waves and high metallic loss specifically at mm-wave bands [1], [2], [3], [4], [5], [6], [7]. Dielectric resonator antennas (DRAs) at mm-wave bands overcome the issue of high losses in metallic antennas and are very efficient radiating elements at such bands. At the sub-6-GHz band, DRAs with high permittivity materials have less overall size compared to conventional metallic ones. Compared to single DRAs, DRA arrays for beam switching/steering as required by 5G and STACOM are less studied in the literature [2], [7], and [8]. In [2], a substrate-integrated DRA array was combined with a 2×4 segmented patch antenna for dual-band operation (at 3.5 GHz and 26 GHz) with beam steering capability. The antenna achieved 11.7% and 12% 10-dB impedance bandwidth and peak gain of 5 and 12.9 dBi at the microwave band and mm-wave band, respectively. The measured beam steering is limited to the range ±25°. In [7], a dual-band antenna with beam steering capability at mm-wave bands is proposed. At the 3.5 GHz band, a low profile (0.03λ) planar inverted-F antenna (PIFA) is used with 10-dB impedance bandwidth of 11.2% (3.28 GHz - 3.67 GHz) and the measured peak gain of 4.8 dBi. At 28 GHz, two 1×6 substrate integrated DRA arrays are designed to support end-fire and broadside beam steering. The maximum simulated beam steering range is ±50° and the measured array gain was 9–10 dBi over the operating band.

None of the designs mentioned designs can cover 5G bands at both sub-6-GHz and mm-waves bands using only a single type of antenna. They combine a DRA with other types of antennas for operating in two well-separated frequency bands. These multi-antenna designs are multilayer structures which adds to the fabrication complexity and their efficiency is low at mm-wave frequencies.

Encapsulated dielectric resonator antennas (E-DRAs) solve these challenges by providing a compact, multi-band, and multi-function solution for future wireless communications. They can cover two bands that are widely separated, such as sub-6-GHz and mm-wave, while also providing beam steering/switching capability at the higher band. Additionally, they offer a reduction in size, fabrication cost, and power consumption compared to traditional metallic antennas. This paper aims to provide a comprehensive study of the current limitations and design challenges of antenna design for future wireless communications and present a novel solution using E-DRAs.

In recent years, additive manufacturing (AM) technologies or so-called 3D printing has received great attention in the antenna research field. The main advantage of AM techniques is the possibility of prototyping complex structures with a reduced cost and with wasting less amount of materials compared to the conventional fabrication techniques [9], [10]. In addition, 3D printing enabled designers to fabricate multi-material 3D structures that may not be easily fabricated with conventional techniques. In addition, 3D printing enables the fabrication of geometrical shapes that could not be simply realized with conventional techniques. In the fabrication of the DRAs, 3D printing enables the ability to tune the relative permittivity of the printed structures by changing the infill percentage (air to solid material ratios). In this work, Fused Filament Fabrication (FFF) additive manufacturing technology is used to realize the proposed E-DRA. FFF technology has been used to fabricate different types of antenna structures [11], [12], [13], [14], [15], [16], [17]. Recently, the possibility of DRA antenna fabrication using FFF has been explored [15], [16], [17], [18], [19], [20], [21]. FFF technology is exploited to fabricate a wideband, low-profile, end-fire dielectric antenna with designable permittivity [15]. In another study, a 3D-printed wideband multi-ring DRA was introduced [17]. A 3D-printed wideband, two-port, dual-frequency DRA was proposed for vehicular communications [21]. In this antenna, an S-band DRA is combined with an X-band dielectric lens antenna. In that structure, only the lower-band element is fabricated with 3D printing. The previous works were not fully realized by 3D printing.

This work presents a novel wideband, high gain, E-DRA element that can cover two widely separated bands at sub-6-GHz and mm-wave. The design methodology enables the systematic design of dual-band DRAs at desired frequency ranges for different applications. The antenna consists of an array of five high-frequency (mm-wave) DRAs embedded into a low-frequency (sub-6-GHz) DRA (used in a switched mode fashion). The FFF 3D printing technique is used to fabricate the whole E-DRA structure with a single material but with different infill, percentages to achieve the required permittivity. The E-DRA is designed to support a wide frequency bandwidth of 33% centered at 3.6 GHz and 27% centered at 30 GHz. The wideband operation over two widely separated bands has not been proposed in previous works. The minimum measured efficiencies were 95% and 80% for sub-6 GHz and mm-wave bands, respectively. The proposed E-DRA provides beam switching capability (five angles within the range ±32°) at the mm-wave band by switching between different small DRA elements.

The paper is organized as follows. The E-DRA structure and operation are briefly described in Section II. In Section III, the design of E-DRA with a single high-frequency element providing a high gain using a lens-shape structure is presented. A complete E-DRA structure with multiple embedded small DRAs operating at the sub-6-GHz and mm-wave band and providing beam steering at the mm-wave band is presented in Section IV. Section V discusses the fabrication of the proposed E-DRA using 3D printing. The measurement and simulation results are

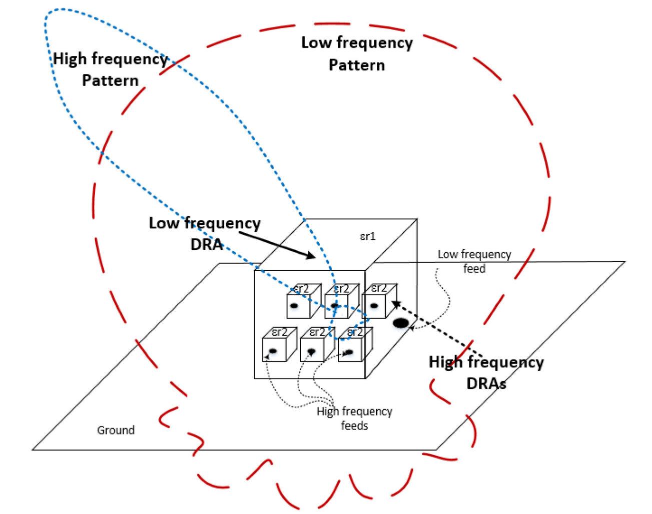

FIGURE 1. The proposed Encapsulated DRA concept.

presented in Section VI. Concluding remarks are given in Section VII.

II. PROPOSED E-DRA IDEA

In this section, we will study the idea of E-DRA by embedding multiple smaller-sized elements with high relative permittivity inside a larger element with lower relative permittivity. This combination allows simultaneous radiation at two widely separated bands and can cover both sub-6-GHz with large DRA and mm-waves with small DRAs. The encapsulated arrays have beam steering capabilities to improve the communication link performance at higher bands. The schematic model of the proposed E-DRA is depicted in Fig. 1, in which the dimensions and feeding of the lower band element are optimized to cover the sub-6 GHz band. The placement, dimensions, separation distances, and feeding of the mm-wave elements encapsulated within the larger elements are optimized for the desired operation at high frequencies.

Different techniques can be exploited to achieve high gain and switching capabilities in antenna configurations; such as utilizing array concepts, conventional reflectors, and lens-based architecture. In this study, we take advantage lens-based method, which is both cost-effective and efficient. A dielectric lens is placed on top of source antennas in order to reshape the spherical wavefront into a planar one [22], [23].

In this work, the larger DRA is providing a directed fixed beam at the lower band. The design is modified to act like a lens for the smaller embedded elements to increase the antenna gain at the higher frequency bands. The beam is properly steered toward a particular direction by selecting one element of the array, and according to its position relative to the lens focal point. There are several different types of dielectric lenses (DL) such as elliptical substrates lenses, spherical lenses, and extended hemispherical lenses [22]. In this work, an extended hemispherical lens is chosen due to its simple structure and minimal required modification in low-frequency DRA to act like a high-frequency lens. The lens is fed by small cDRAs at mm-wave band and is a part of the DRA antenna for sub-6-GHz. Moreover, by switching between multiple feeds to generate steered beams at mm-wave band.

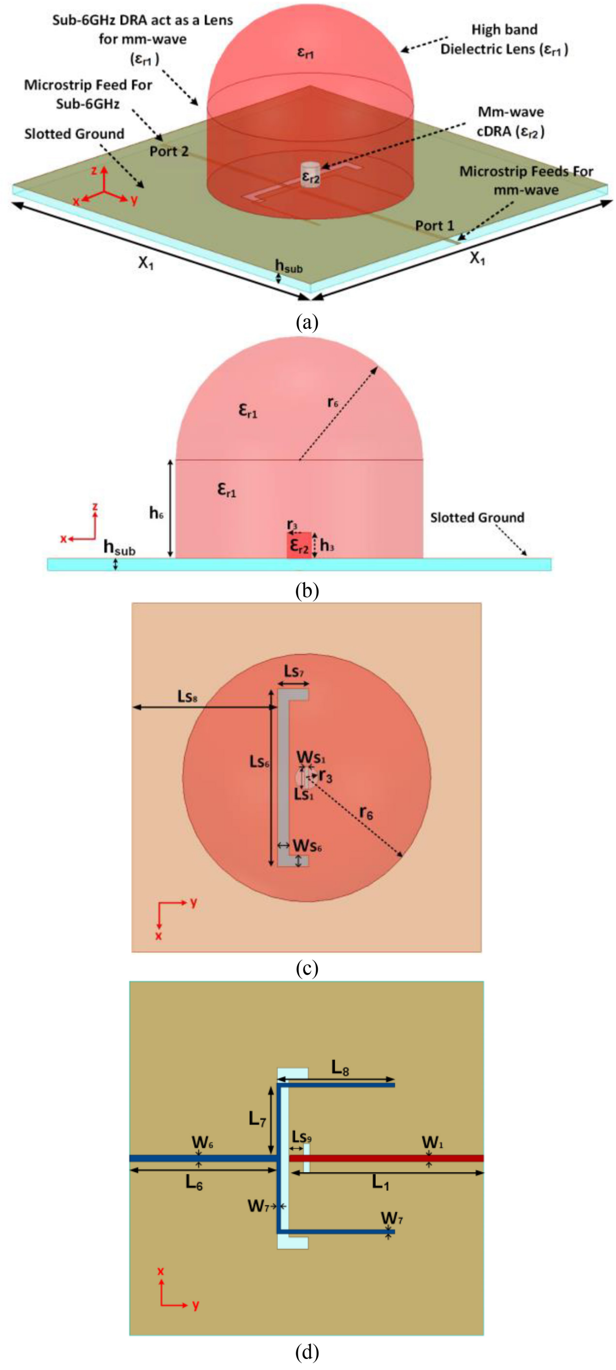

FIGURE 2. Geometry of proposed differentially fed SIC backed cDRA. (a) Top view (b) Cross-section from side view (c) Perspective view.

III. DESIGN OF THE E-DRA WITH SINGLE EMBEDDED ELEMENT

Figure 2 shows the E-DRA structure in which a smaller cDRA is embedded into a larger cDRA. A DL is placed on top of the larger cDRA. At the mm-wave band, the smaller DRA acts as a radiator while the larger DRA in conjunction with the DL forms an extended hemispherical lens and enhances the gain. Both the large DRA and the DL have a relative permittivity of ε_{r1} and the smaller DRA has a relative permittivity of ε_{r2} where in general $\varepsilon_{r1} < \varepsilon_{r2}$.

The design procedure involves the selection of the substrate material for feeding the E-DRA, where we use Rogers RT/duroid® 5880 as the substrate and the cDRAs will be assembled on top of it. The substrate material is a low loss material with nominal dielectric constant and loss tangent of 2.2 and 0.0009, respectively. At sub-6-GHz, the DRA is fed by a fork-shaped feed network at the bottom of the substrate (Fig. 2(d)), which excites the $HEM_{11\delta}$ mode of the large DRA through power coupling via a C-shaped slot on the top metal surface of the substrate (Fig. 2(c)) which provides broadside radiation. This kind of feed network offers maximum gain at the central frequency [24]. The C-shaped slot is at an offset ($= L_{s9}$) from the center, which has a negligible effect on the pattern at sub-6 GHz band. The mm-wave linear slot, feeding the small cDRA is at the center of the top metallic layer of the substrate and its dimensions are specified by L_{s1}, and W_{s1} (Fig. 2(c)). A 50-Ω microstrip line with a width of W_1 and a length of L_1 is also used to feed the slot as shown in Fig. 2(d).

In the next step, E-DRA materials are selected based on the required bandwidth. The dielectric constant of the resonator affects the bandwidth and size of the DRA antenna. In this design, the whole E-DRA has been 3D printed using FFF technology with commercial filament PREPERM 3D ABS DK 12.0 (from company Avient based in Belgium) with nominal relative permittivity of 12.0 ± 0.5 and loss tangent of 0.0029 at 2.4 GHz. The relative permittivity can be controlled by the infill percentage during the 3D printing process as detailed in Section V. The relative permittivity of DL and the larger DRA (ε_{r1}) is chosen to be 4. A lower value for relative permittivity increases the overall DRA size and a larger value negatively affects the performance of mm-wave embedded elements due to the increased reflection within the larger DRA and lens. The relative permittivity of the smaller DRA (ε_{r2}) is chosen to be 9 since this is the maximum relative permittivity that can be achieved by ABS1200 through FFF 3D printing scheme at mm-wave frequencies.

Dimensions of the larger DRA are estimated by the design procedure described in [25]. For a cDRA, the resonant frequency of the fundamental mode ($HEM_{11\delta}$) can be approximated using the formula:

$$f_{HEM11\delta} = \frac{6.324c_0}{2\pi r\sqrt{\varepsilon_r + 2}}\left(0.27 + 0.36\left(\frac{r_6}{2h}\right) + 0.02\left(\frac{r_6}{2h}\right)^2\right), \quad \left(\text{for } 0.4 \le \frac{r_6}{2h} \le 6\right). \tag{1}$$

where r_6 is the cDRA radius, h is DRA height in Fig. 3 and c_0 is the speed of light in free space. For the larger DRA, ε_r is equal to ε_{r1} in Eq. (1).

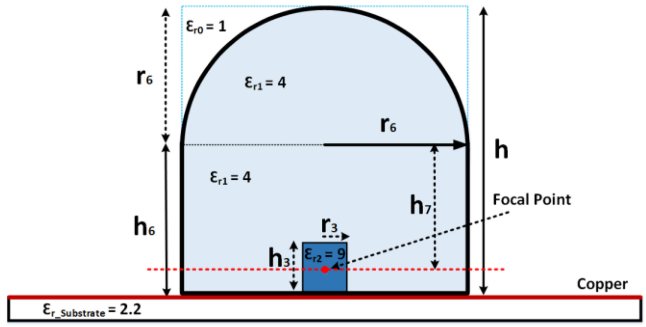

FIGURE 3. Single element E-DRA from view side.

Assuming an extended hemispherical lens with the same radius as the DRA shown in Fig. 3(a), the optimum size of the lens extension without the embedded small cDRA, h_6 ($= h - r_6$) is approximated by [26]:

$$h_6 = h - r_6 = r_6\left(\frac{\sqrt{\varepsilon_{r1}} + 1}{\sqrt{\varepsilon_{r1}} - 1} - 1\right). \tag{2}$$

For the selected permittivity ($\varepsilon_{r1} = 4$) the equation will reduce to $h_6 = h - r_6 = 0.73r_6$. If $f_{HEM11\delta} = 3$GHz (the lowest frequency at the desired sub-6-GHz band) and $\varepsilon_{r1} = 4$, r_6 will be 15.5 mm according to (1) and h and h_6 will be calculated as 26.9 mm and 11.4 mm according to (2). The focal length of the lens slightly reduces due to the larger permittivity, in presence of the small cDRA. h_7 in Fig. 3 is the focal point of the lens for the extended hemispherical lens with small embedded cDRA. In this design, the small cDRA inside the bigger cDRA is the feed for the lens at mm-wave band, so the middle of the small cDRA is approximately assumed to be the focal point. Consequently, half of the height of the small cDRA ($h_3/2$) must be added to the value of $h_6 (= h_7 + \frac{h_3}{2})$ derived before and the total height of the larger DRA with DL will be calculated as $h = h_7 + r_6 + h_3/2$.

At the mm-wave band, the $HEM_{11\delta}$ mode is also excited inside the smaller DRAs (in this case, the larger DRA surrounding the smaller one acts as a lens). Equation (1) is valid where the background medium is free space. To find the dimensions of the DRA with a relative permittivity of ε_r embedded in background medium with relative permittivity of ε_b, ε_r in (1) can be replaced by $\varepsilon_r/\varepsilon_b$. We assumed that the background medium has the permittivity of $\varepsilon_b = \varepsilon_{r1}$ (due to the small size of mm-wave cDRA compared to sub-6GHz DRA) so that we can calculate an initial value for the dimensions of the smaller cDRA. The initial value of h will be 28.6 mm assuming that the relative permittivity of $\varepsilon_{r2} = 9$ for the small cDRA, the height (h_3) and radius (r_3) of the small cDRA are 3.5 mm and 1.7 mm, respectively according to (1).

The initial values for the large cDRA, DL, and the small cDRA (h_6, r_6, h_3, and r_3) are optimized using full-wave simulations in HFSS to obtain wide impedance bandwidths at both sub-6-GHz and mm-wave bands. Fig. 4 shows the reflection coefficient of the antenna versus frequency for

TABLE 1. Optimum geometrical values for the single element E-DRA.

Parameter	Value (mm)	Parameter	Value (mm)
X1	75	hsub	0.254
h6	12.4	r6	16.2
h3	3.3	r3	1.5
Ws1	0.25	Ls1	2.6
Ws6	1.5	Ls6	23
Ls7	4	Ls8	33.5
W1	0.78	L1	39.65
W6	0.78	L6	33.5
W7	0.19	L7	8.89
L8	13	Ls9	2.2

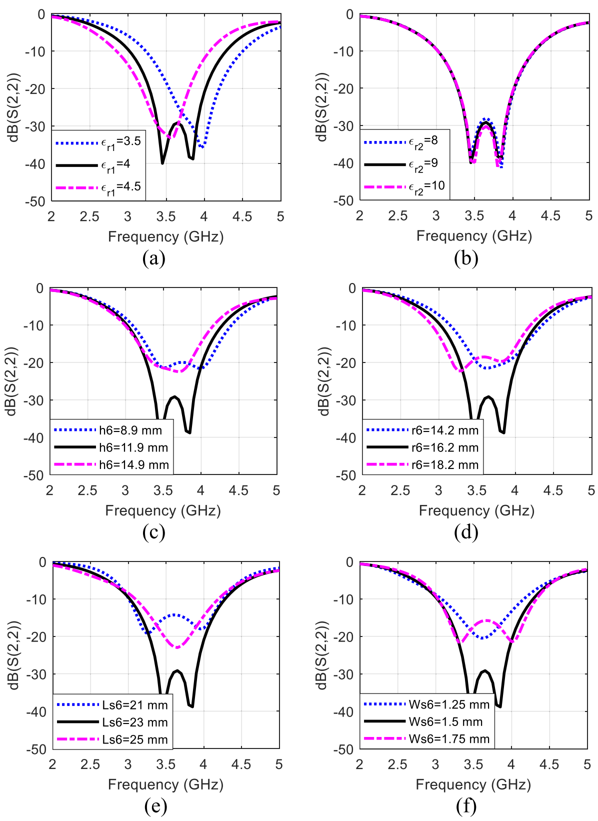

FIGURE 4. Reflection coefficient of the antenna at sub-6-GHz band versus frequency for different values of (a) ε_{r1}, (b) ε_{r2}, (c) h_6, (d) r_6, (e) L_{s6}, and (f) W_{s6}. Other parameters are set according to the values provided in Table 1.

different values of ε_{r2}, ε_{r1}, h_6, r_6, L_{s6}, W_{s6} and L_{s6} at the sub-6-GHz band. These results are for E-DRA with $\varepsilon_{r1} = 4$ and $\varepsilon_{r2} = 9$. Other parameters are set according to the values provided in Table 1. As shown in Fig. 4(a), the relative permittivity of the small cDRA (ε_{r2}) does not affect the reflection coefficient at sub-6-GHz; however, the relative permittivity of the large DRA (ε_{r1}) and its size (h_6 and r_6) control the reflection coefficient. Figs. 4(b)-(d) also shows, smaller ε_{r1}, larger h_6, or larger r_6 shifts the operation band to higher frequencies. In addition, a fork-shaped feed network can be tuned for better matching (Fig. 4(e)-(g)).

Optimization is done at mm-wave frequency considering the radiation pattern and reflection coefficient of cDRAs. In Fig. 5, we can observe that the reflection coefficient of the

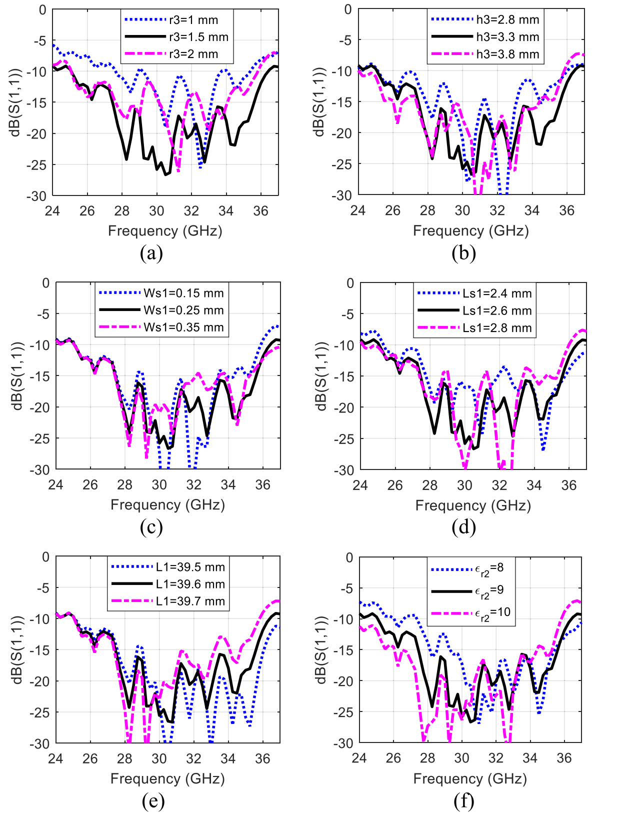

FIGURE 5. Reflection coefficient of the antenna at mm-wave band versus frequency for different values of (a) r_3, (b) h_3, (c) W_{s1}, (d) L_{s1}, (e) L_1, and (f) ε_{r2}. Other parameters are set according to the values provided in Table 1.

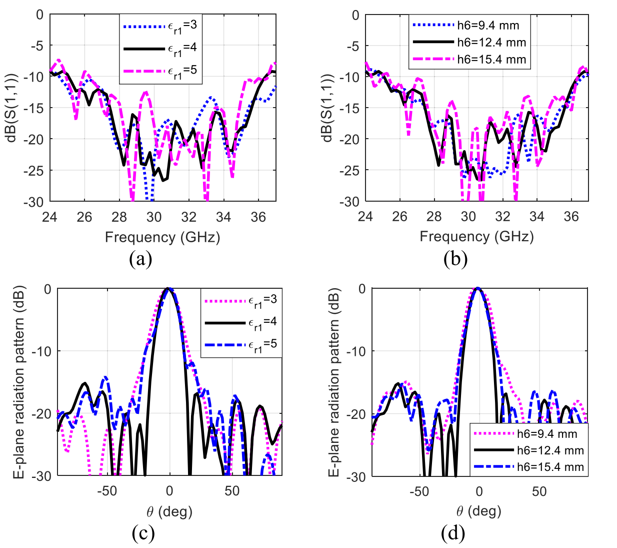

FIGURE 6. Reflection coefficient of the antenna at mm-wave band for different ε_{r1} (a) and different h_6 (b). Pattern at 30.75 GHz (mm-wave band) for different ε_{r1} (c) and different h_6 (d). Other parameters are set according to the values provided in Table 1.

small cDRA is mainly affected by its relative permittivity and size. At the same time, the pattern at the mm-wave band is mainly affected by the relative permittivity of the larger DRA, the DL, and the length of the extended hemisphere (Fig. 6c-d). Other parameters are set according to the values provided in Table 1. We can observe in Figs. 4 and 5 that the simulation shows a 10-dB return loss bandwidth of 35.6% centered at 3.65 GHz (3-4.3 GHz) and 36.7% centered at 30.75 GHz (25.1-36.4 GHz).

IV. DESIGN OF THE E-DRA WITH A MM-WAVE ARRAY

In this section, the design of single element E-DRA presented in Section III is modified to act as a beam steerable antenna. The steering capability has been investigated for automotive radar and millimeter-wave high-data-rate point-to-point links [27]. As reported in [28] and [29], extended hemispherical lenses with switched focal plane arrays provide significant advantages such as maximum beam coverage with a minimum number of elements in beam scanning applications. The antenna lateral offset position with respect to the lens focal point determines the scan angle. In the case of extended hemispherical lenses, the relationship is given by [27]:

$$\tan(\theta_s) = \frac{d}{h_7} \tag{3}$$

where θ_s is the scan angle, d is the element lateral offset from the focal point and h_7 is the focal length with small embedded cDRA. The initial value for d is set to 3.3 mm in order to cover the beam steering range of $\pm 32^{\circ}$ at the mm-wave band ($\theta_s = 16^{\circ}$ and $h_7 = 11.4\ mm$).

Fig. 7(a) shows the disassembled E-DRA with beam steering capability. As shown in Fig. 7(b), an array of five elements is embedded inside the larger cDRA and the DL to enable beam steering at the mm-wave band. Each of the five small cDRAs is fed separately by a 50-Ω microstrip line and a slot with the same initial width as presented in Section III (Fig. 7(c) and (d)). At sub-6-GHz, the DRA is fed by a fork-shaped feed network at the bottom of the substrate with the same initial size as in Section III (Fig. 7(c)). The mm-wave feeding slots are at the center of the top metal of the substrate in the y-direction with a separation of d in the x-direction. Their dimensions are optimized for best matching at the mm-wave band for each port (Fig. 5(d)). The elements with the same distance from the center in the x-direction have the same matching response due to the symmetry of the structure and feed. The substrate used is RT/duroid 5880 with a thickness of 10mm. An aluminum plate with a thickness of 2 mm is added to the structure to improve mechanical stability. Six connectors (one for sub-6-GHz and five for mm-wave band) are used to feed the elements. Initial values for the dimensions of the larger and smaller cDRAs are the same as the ones for single-element E-DRA presented in Section III. These values need to be fine-tuned by full-wave simulation to obtain desired characteristics (pattern and, impedance match). During the optimization, the aluminum plate is also included in the structure as shown in Fig. 5(a). Positions of the small DRAs are also fine-tuned to give the best performance in terms of low side lobes level (SLL) when switching the beam. Finally, the optimum geometrical parameters are listed in Table 2. The reflection coefficient curves are presented in Section VI.

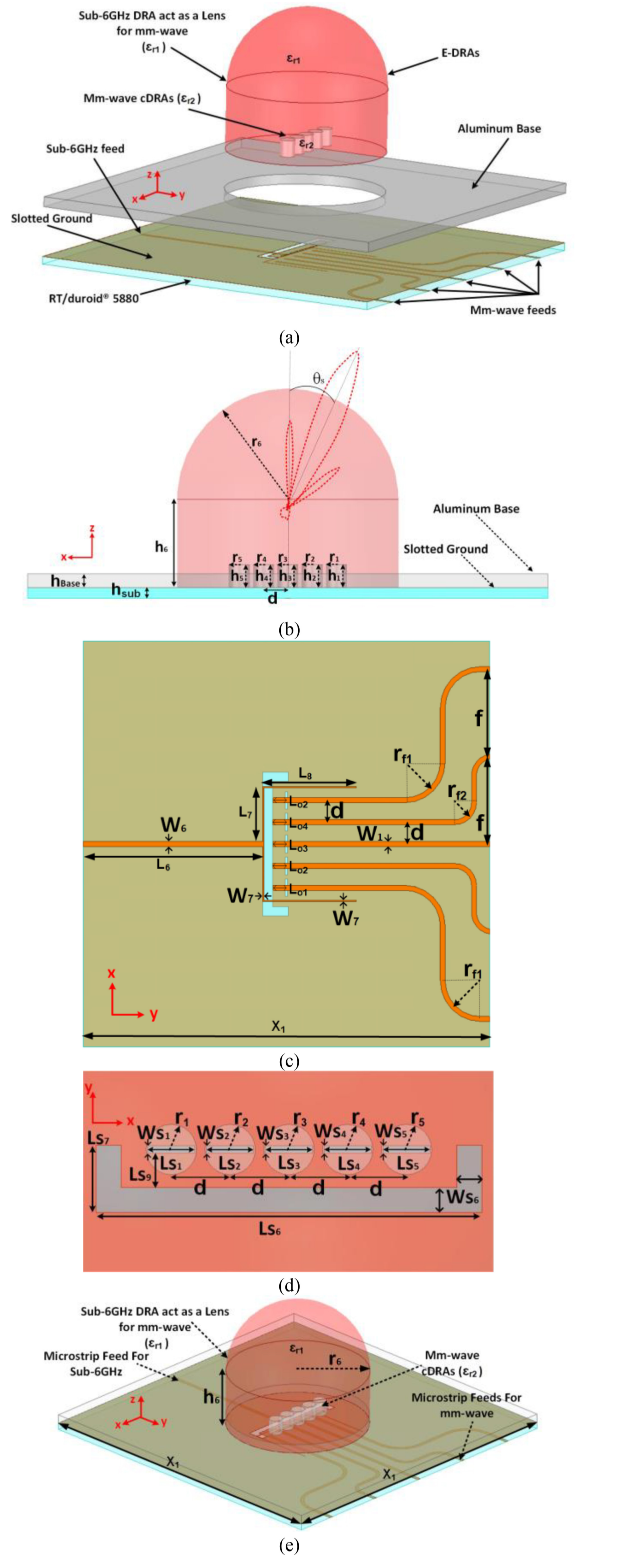

FIGURE 7. E-DRA with beam steering capability at mm-wave band: (a) disassembled antenna, (b) side view, (c) bottom view, (d) top view of slots, and (e) perspective view.

TABLE 2. Optimized values for different geometrical parameters in the E-DRA with beam steering capability.

Parameter	Value (mm)	Parameter	Value (mm)
X_1	75	h_{sub}	0.254
h_6	12.7	r_6	16
$h_{1,2,3,4,5}$	3.3	$r_{1,2,3,4,5}$	1.5
$W_{s1,s2,s3,s4,s5}$	0.45	$L_{s1,s5}$	3.1
$L_{s2,s4}$	3	L_{s3}	2.6
W_{s6}	1.5	L_{s6}	23
L_{s7}	4	L_{s8}	33.5
W_1	0.78	$L_{o1,o5}$	2.1
L_{o3}	2.15	$L_{o2,o4}$	2.2
W_6	0.78	L_6	33.5
W_7	0.19	L_7	8.89
d	3.5	h_{Base}	2
f	14	r_{f1}	5.7
r_{f2}	2.7		

This proposed antenna can be designed for any application requiring more than 25% impedance bandwidth at sub-6-GHz and mm-wave bands. The introduced 5G antenna in this paper is a proof of concept and can support n48, n77, and n78, 5G bands at sub-6-GHz and n257, n258, and n261 bands at for mm-wave.

V. FABRICATION OF THE E-DRA

The proposed E-DRA design was prototyped using an extrusion-based AM technology, called FFF. In this method, a polymer-based filament is fed into a hot nozzle, where it is extruded in a molten state and deposited in the form of desired geometry in a layer-by-layer fashion. FFF enables the fabrication of the entire dielectric antenna as a single piece with the same material and provides higher control over permittivity by adjusting the infill percentage.

The FFF process in its nature is line-by-line and layer-by-layer deposition, which makes it different from fabrication methods like casting and molding, and results in gaps between deposited lines and layers in solid samples. Subsequently, the density of the printed parts is different from the raw material. This difference in relative density leads to a lower than the nominal actual permittivity of the 3D printed samples even for the 100% infill. As a result, the relative permittivity of the printed samples highly depends on the infill percentage and is always less than the nominal permittivity of the filament (Fig. 8e).

In this work, the E-DRA was printed using a commercial Prusa i3 MK3S+ FFF 3D printer. The material is commercial PREPERM ABS1200® filament, which is a special compound produced by Premix proprietary ABS technology, which is a relatively low loss material. cDRA samples with different sizes and infill percentages were fabricated (Fig. 8(a)) to obtain the relationship between the relative permittivity of the 3D printed parts and different infill percentages and sizes. The infill pattern of the fabricated cDRA is rectilinear, in which the deposition direction in each layer is normal to that of the preceding layer.

In the proposed antenna design, the larger DRA and the DL are fabricated with an infill percentage of 50% to

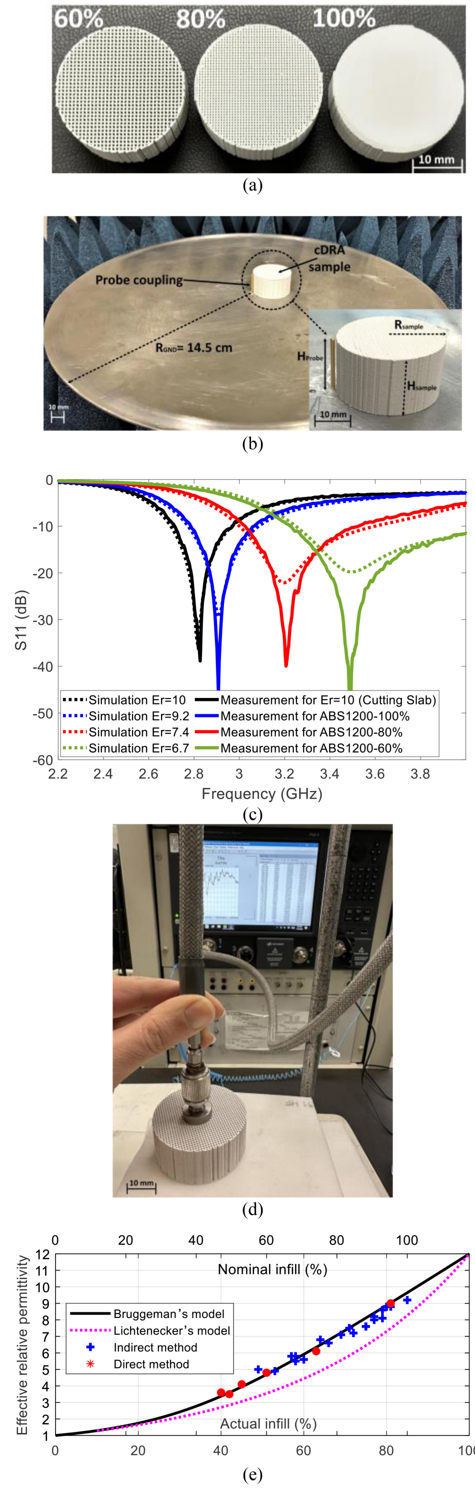

FIGURE 8. (a) Fabricated cDRAs with different infill percentages. (b) Indirect measurement of permittivity by probe coupling (c) Reflection coefficient obtained through experiment and simulation for different infill percentages (indirect measurement) (d) Direct Measurement of relative permittivity of 50% nominal infill cDRA with coaxial probe. (e) Effective relative permittivity measured with two different methods for samples.

obtain a relative permittivity of 4 and the smaller embedded DRAs are fabricated with a maximum 100% infill to obtain a relative permittivity of 9. The 3D printer settings and

TABLE 3. FFF-3D printing parameters.

Extrusion temperature (°C)	Printing speed (mm/s)	Infill pattern	Layer height (mm)	Nozzle diameter (mm)
280	30	Rectilinear	0.1	0.4

parameters are selected according to the filament manufacturer's instructions to minimize the defects in the 3D printed samples. A summary of these settings is listed in Table 3. The extrusion temperature is 20°C higher than the temperature recommended by the filament manufacturer to avoid nozzle clogging during the printing process. In addition, no solid layer is printed on top or bottom of the samples and no vertical shells are added to the side of the samples to maintain uniform permittivity throughout the sample. Figure 9(a) shows a unit cell model of the rectilinear fill pattern. Each unit cell includes 5 layers and from top to bottom layer, each layer is rotated by 90° in clockwise direction with respect to the last layer (so, layer 1 and 5 are the same). 3D printing parameters determine the width of the lines and spacing between the layers (L_{P1}, L_{P2}, W_{P1}, W_{P2}, H_{P1}), and the infill percentage determines the dimensions of the voids (W_{h1}).

The relative permittivity of the samples is measured by indirect and direct methods. In the indirect method, the DRAs with different sizes (R_sample=7.1, 8.7, 13.2, and 14.5 cm and H_sample=7.3, 6.4, 20.6, and 16.5 cm) are fed by a probe ($H_{Probe} = 1.5,\ \ and\ 1.11\ cm$) from the side (Fig. 8(b)) and the measured reflection coefficient is compared to the simulated one to find the relative permittivity. The distance between probe and cDRAs is less than 0.5 mm and tuned in the measurement process based on the dimension and permittivity of the cDRAs. A cDRA sample is also fabricated by CNC machining (tolerance of 0.02 mm) of C-Stock AK for the purpose of calibration. While the final size of the machined sample is the same as 3D printed cDRAs, the former's nominal relative permittivity is 10, and loss tangent equals 0.002. In the next step, we simulated the response of a bulk homogeneous material with the same size and shape as the measured cDRA placed on a ground plane and fed by the same probe, using the simulation techniques explained in Section III. Then, we performed a systematic study to find the relative permittivity of the cDRA by fitting different values of relative permittivity in the simulation. The simulation results for different permittivity values are compared with the experimental analysis to find the matching relative permittivity value, as shown in Fig. 8(c).

In the direct method, a coaxial probe on large-size cDRAs ($R_{sample} = 3\ cm\ and\ H_{sample} = 2.5\ cm$) is used as shown in Fig. 8(d). The permittivity of the sample is measured by changing the probe position and the final value is considered as an average of the result of the five measurements. The bottom and top surfaces of the DRAs are sanded to ensure direct contact between the dielectric part and the ground/probe.

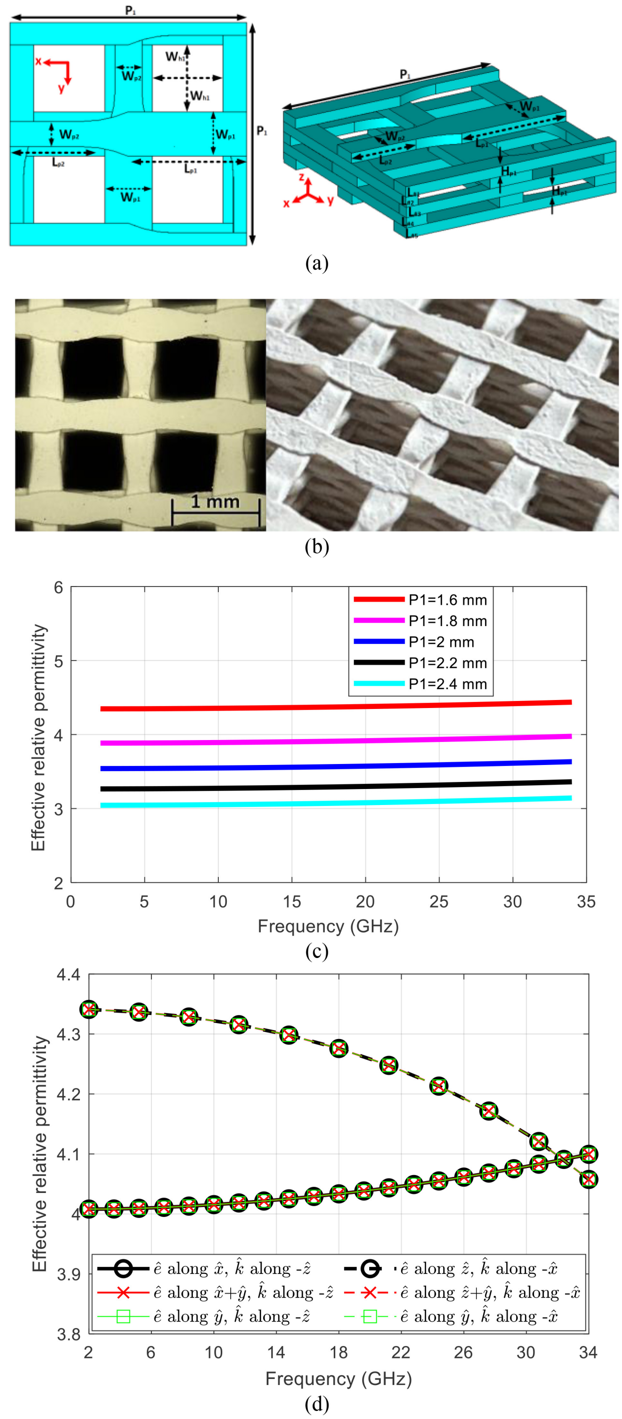

FIGURE 9. (a) Simulated rectilinear Unit cell and (b) Fabricated rectilinear pattern (c) Simulated effective relative permittivity for different value of P_1 (d) Simulated effective relative permittivity for the unit cell in (a) seen by plane waves polarized along $\hat{e}$ and propagating along $\hat{k}$.

Figure 8(e) depicts direct and indirect relative permittivity measurement results with respect to nominal and actual infill percentages. The nominal infill percentage is the value set in the print settings, which determines the distance between extruded lines in 3D printing slicing software. The actual infill is obtained by dividing the samples' actual

TABLE 4. Optimum geometrical values for unit cell (actual infill 40%).

Parameter	Value (mm)	Parameter	Value (mm)
P_1	2.2	H_{P1}	0.1
L_{P1}	1.1	W_{P1}	0.41
L_{P2}	0.8	W_{P2}	0.31
W_{h1}	0.69		

weight by the weight of fully solid samples (calculated from the material's density and the solid sample's volume). As observed, the relative permittivity decreases from a maximum value of 9 to 3.5 when the nominal infill percentage is varied from 100% to 45%. Comparing measurement results with Bruggeman's [30] and Lichtenecher's [31] models (Fig. 8(e)), it can be concluded that Bruggeman's model is more accurate in predicting the relative permittivity of our 3D printed parts. Bruggeman's model is applicable to a dielectric mixture that consists of two different uniformly distributed materials. According to the Bruggeman relation, the effective relative permittivity (ε_{eff}) of samples with two components (here, the filament material and the air) can be obtained using:

$$\left(1 - v_{filament}\right)\frac{\varepsilon_{air} - \varepsilon_{eff}}{\varepsilon_{air} + 2\varepsilon_{eff}} = -v_{filament}\frac{\varepsilon_{filament} - \varepsilon_{eff}}{\varepsilon_{filament} + 2\varepsilon_{eff}} \quad (4)$$

in which, $\varepsilon_{filament}$ and ε_{air} are the permittivities of the filament and the air, respectively. $v_{filament}$ is the volume fraction of filament in the total volume of the structure. For any sample, $v_{filament}$ can be calculated from:

$$v_{filament} = \frac{\rho_{actual}}{\rho_{solid}} \quad (5)$$

where ρ_{solid} is the density of filament and ρ_{actual} is the density of the 3D-printed sample. The density of the actual filament (as received from the filament manufacturer) is measured by Gas Pycnometer (AccuPyc 1340 Folio Instrument) and equals 2.55 ± 0.02 g/cm^3, which is approximately 10% more than the value provided by the filament manufacturer (2.37 g/cm^3).

A periodic structure with a unit cell made of ABS1200 (ε_r = 12) and rectilinear pattern is simulated in CST Microwave Studio (using master-slave boundaries). For the unit-cell, the line width and the layer height are fixed. The simulation results for effective permittivity versus frequency for different P_1 values are shown in Fig. 9(c). Based on the results, a P_1 of 2.2 mm is selected for fabrication, and this is equivalent to infill of 40%. Other geometrical parameters of the unit cell are listed in Table 4. Figure 9(b) shows an image of a fabricated unit cell with the actual infill of 40%. Figure 9(d) shows the simulated effective relative permittivity for the unit cell shown in Fig. 9(a) with P_1 = 1.87 mm while the unit cell is illuminated by plane waves with different polarizations $(\widehat{e})$ and different directions of propagation $(\widehat{k})$. It can be observed that the obtained values for different cases are very close to each other and so the unit cell can be considered as an isotropic effective medium.

The dimensional precision and surface quality of 3D printed samples can vary depending on the technology and

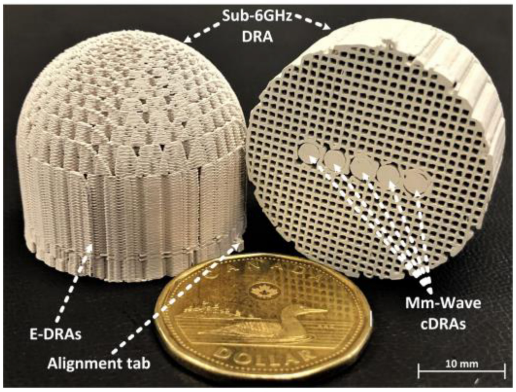

(a)

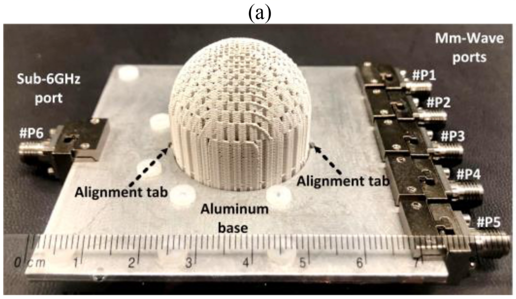

(b)

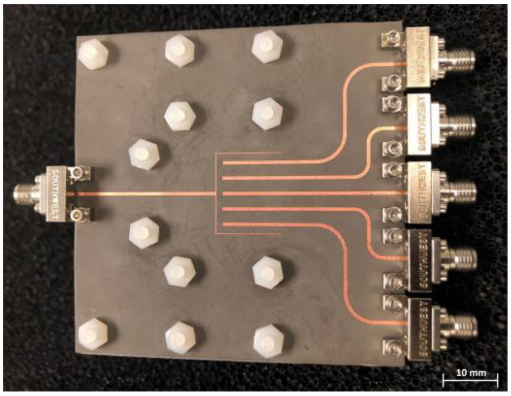

(c)

FIGURE 10. (a) 3D printed E-DRA fabricated from ABS1200 with rectilinear infill pattern. (b) Image of the antenna. (c) Feed network on the back side.

method used. In general, the dimensional accuracy of FFF 3D printing varies between 0.005mm to 0.1mm [32], which is not as precise as some traditional manufacturing methods such as CNC machining or injection molding. The resolution of a 3D printer, or the minimum size of the features it can print, is an important factor affecting the dimensional accuracy of the final printed samples. Additionally, the type of material being used and the ambient conditions during printing can impact the accuracy of the final product. In the current study, the height resolution of the 3D printer is 0.1mm; At the same time, the in-plane resolution of the 3D printers is 0.02mm according to the manufacturer, which is higher than the height resolution and enables us to fine-tune the relative distance of the embedded DRAs. This relatively fine in-plane resolution makes possible the precise

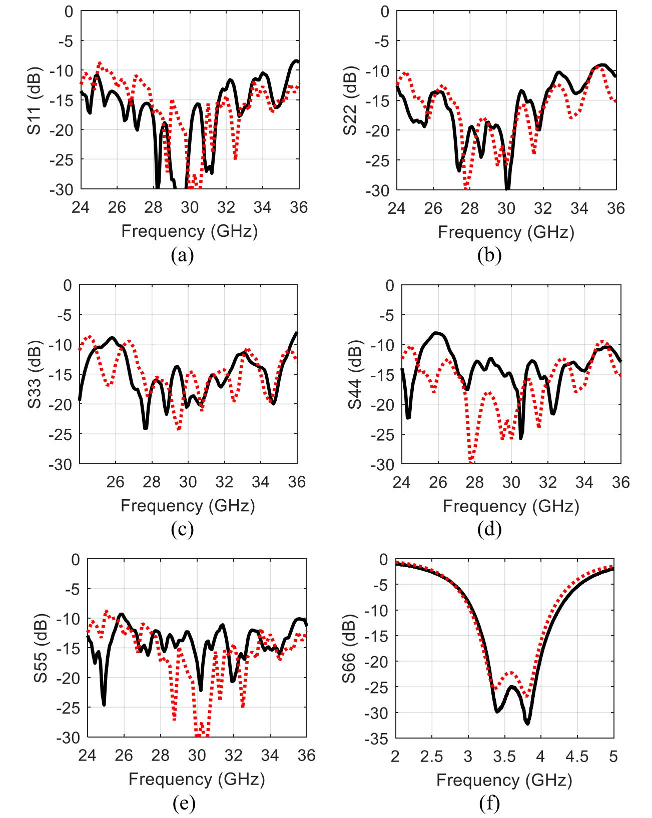

FIGURE 11. Simulated (dashed line) and measured (solid line) reflection coefficient for the E-DRA, (a) port 1, (b) port 2, (c) port 3, (d) port 4, and (e) port 5 at mm-wave and (f) port 6 at sub-6-GHz (port numbers are indicated in Fig. 9(a)).

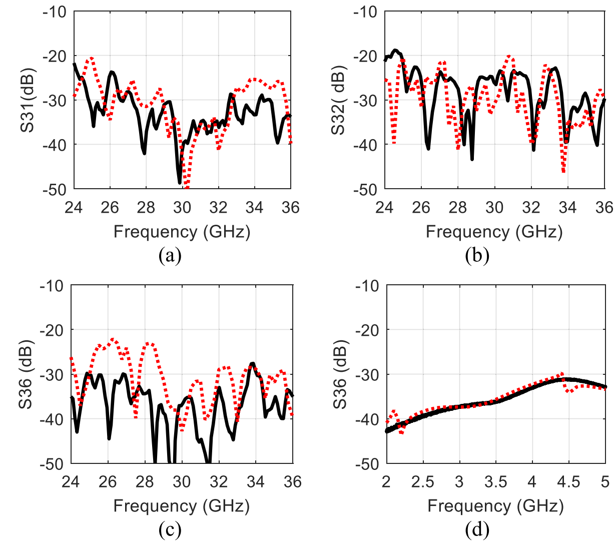

FIGURE 12. Simulated (dashed line) and measured (solid line) coupling between different ports: (a) port 3-port 1, (b) port 3-port 2, (c) port 3-port 6 at mm-wave, and (d) port 3-port 6 at sub-6-GHz (port numbers are indicated in Fig. 9(a)).

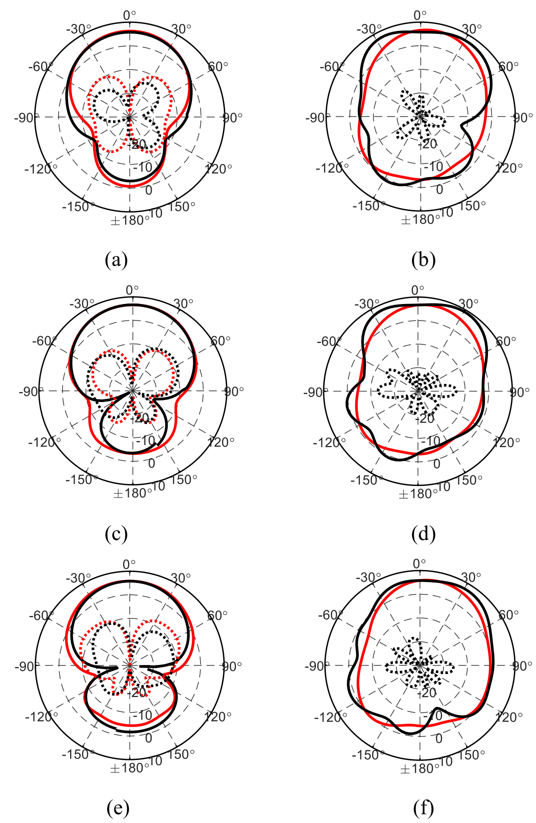

FIGURE 13. Measured and simulated co/cross polarization radiation patterns for the proposed antenna: (a) 3 GHz at H-plane, (b) 3 GHz at E-plane, (c) 3.6 GHz at H-plane, (d) 3.6 GHz at E-plane, (e) 4.2 GHz at H-plane, and (f) 4.2 GHz at E-plane.

positioning of the small DRAs inside the larger DRA with different relative permittivity.

VI. SIMULATION AND MEASUREMENT RESULTS

The designed dual-band E-DRA was simulated in ANSYS HFSS at both sub-6-GHz and mm-wave frequency bands. The final dimensions of the fabricated E-DRA are shown in Table 2. Figure 10 shows the images of the fabricated antenna with 3D-printed DRA parts. Alignment tabs are included on both sides of the E-DRA and the aluminum base (Fig. 10(a,b)) to reduce the placement error in the DRAs on the feeding slots. The DRA is attached to the substrate using a very thin layer of epoxy glue (this layer was included in the simulation model). The feed network at both frequency bands is shown in Fig. 10(c).

The antenna is measured by a Satimo Starlab near-field system at the sub-6-GHz band, and an MI Technologies Compact Range Chamber at the mm-wave band at the Poly-Grames research center. The results of the measured and simulated reflection coefficients of the antenna are shown in Fig. 11. A good match can be observed between the results of both methods. The measured -10-dB reflection coefficient bandwidth is 33%, (centered at 3.6 GHz) for the sub-6-GHz band and 27%, (centered at 30.5 GHz) for the mm-wave band. The achieved operation bandwidths at both bands are the highest among the previous works with dual-band DRA antennas for 5G applications. As shown in Fig. 12, the measured isolation between the antenna ports is better than 31 dB and 25 dB at sub-6-GHz and mm-wave bands, respectively.

The simulated and measured co/cross-polarization radiation patterns of the antenna at E- and H-planes (normalized

TABLE 5. Comparison of the proposed E-DRA with recent dual band antennas covering both sub-6-GHz and mm-wave bands.

Reference	This work	[1]	[2]	[5]	[6]	[7]
Center Frequency (GHz)	3.6/30.5	3.5/28	3.5/26	3.5/28	5.8/29.2	3.5/28
Frequency Ratio	8.47	8	7.42	8	5.03	8
Measured BW (|S11|<-10 dB) %	33/27	20.7/20.5	11.7/11.9	4/12.5	3.5/4.6	11.2/13.8
Max. Measured Gain (dBi)	7.2/18	7/11.3	5/12.9	2.5/9.8	10.9/18.7	4.8/10.8
Antenna type (Sub-6-GHz/mm-wave)	DRA/DRA	Dipole /Yagi	Patch/SIDRA	Slot/Slot	patch /Slot	Patch/SIDRAs
Array (sub-6-GHz/mm-wave)	No/No	Yes/Yes	Yes/Yes	No/Yes	Yes/Yes	No/Yes
Antenna Size (*/λ_0^3)	$0.87 \times 0.87 \times 0.35$	$0.5 \times 0.4 \times 0.03$	$0.41 \times 0.3 \times 0.03$	$0.85 \times 0.1 \times 0.13$	$1.55 \times 1.35 \times 0.04$	$0.45 \times 0.3 \times 0.03$
Min. Antenna Efficiency (%)	95/80	$-/-$	$-/-$	90/75	73/41	$-/-$
Beam Steering Capability (measured)	±32°	+25°	±25°	±30°	No	–

*λ_0 is the free-space wavelength at the center frequency of the lower band.

to the maximum of the co-polarization) and at 3, 3.6, and 4.2 GHz (sub-6-GHz band) are shown in Fig. 13.

The simulated and measured co/cross-polarization radiation patterns of the antenna at E- and H-planes (normalized to the maximum of the co-polarization) and at 28, 30, and 32 GHz (mm-wave band) are shown in Fig. 14 for broadside pattern (where only the center small DRA, i.e., the port 3, is fed). The cross-polarization level is smaller than -20 dB at all mm-wave frequencies for the broadside and a good agreement can be observed between the measured and simulated results. It can be observed that in all cases, SLL is smaller than -12 dB and -13 dB at the E-plane and H-plane, respectively. The antenna pattern is stable in the whole bandwidth. Figure 15 shows the simulated and measured steered radiation patterns at 28, 30, and 32 GHz. The beam is steered at 5 discrete angles in the range ±32° with SLL larger than 10 dB and gain larger than 14 dBi by feeding different small cDRAs. The scan loss at ±32° is 2, 3, and 3.5 dB at 28, 30, and 32 GHz, respectively.

Figure 16 shows the measured and simulated realized gain at broadside direction versus frequency at sub-6-GHz and mm-wave bands. In the case of sub-6-GHz band, the maximum measured gain is 7.2 dBi at 3.2 GHz and in the case of an mm-wave band, the maximum measured gain is 18 dBi at 31.5 GHz. As shown in Fig. 17, the measured efficiency is more than 80% over the mm-wave band (26.5-34.5 GHz) and 95% over the sub-6-GHz band (3-4.2 GHz).

A comparison of this work with recent dual band antennas covering both sub-6-GHz and mm-wave bands (for 5G application) is made in Table 5. The proposed antenna has the highest bandwidth at both sub-6-GHz and mm-wave bands while its DRA part is completely fabricated by 3D printing. The antenna is made of low-loss dielectric materials and thus it exhibits a high radiation efficiency at both bands compared to the other works.

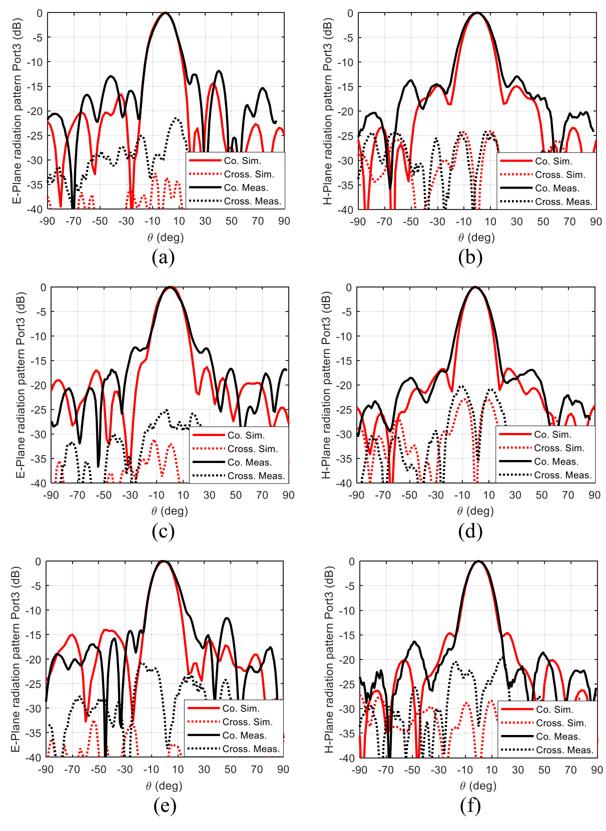

FIGURE 14. Measured and simulated co-/cross polarization radiation patterns at E- and H-planes: (a) 28 GHz at E-plane, (b) 28 GHz at H-plane, (c) 30 GHz at E-plane, (d) 30 GHz at H-plane, (e) 32 GHz at E-plane, (f) 32 GHz at H-plane.

VII. CONCLUSION

Encapsulated DRAs (E-DRAs) as a novel dual wide-band DRA structure are proposed for operation at sub-6-GHz and mm-wave frequency bands with a high-frequency ratio. The sub-6-GHz DR also acts as a dielectric lens for the

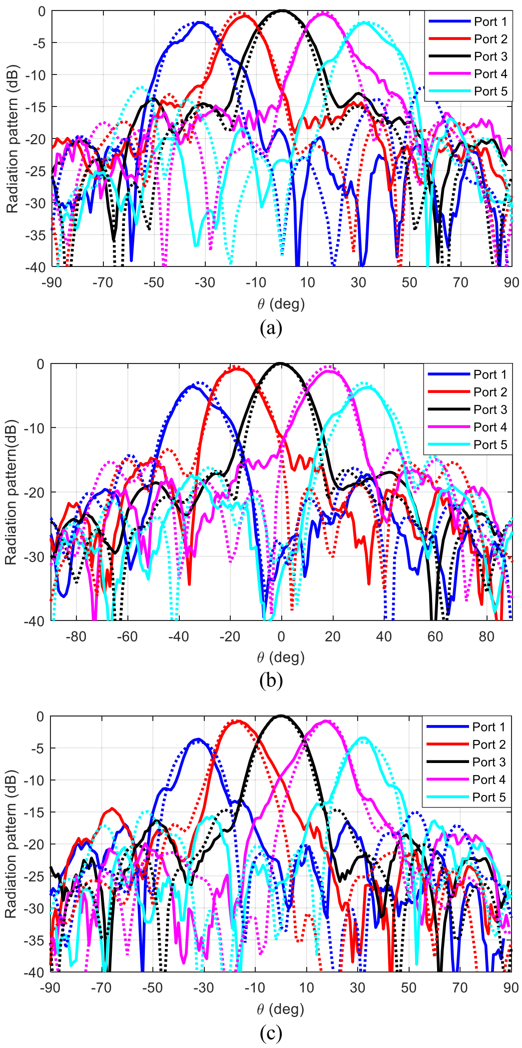

FIGURE 15. Normalized measured (solid line) and simulated (dashed line) steered radiation patterns for the cDRA at port 3 at (a) 28 GHz, (b) 30 GHz, and (c) 32 GHz.

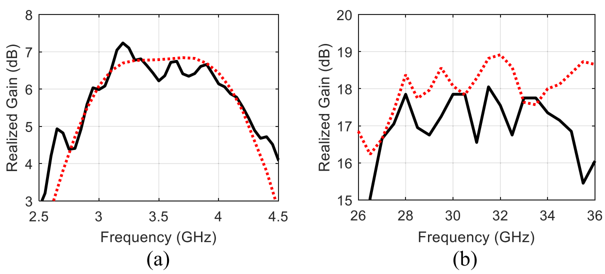

FIGURE 16. Measured (solid line) and simulated (dashed line) realized gain at (a) Sub-6-GHz and (b) mm-wave band.

mm-wave DR to enhance the gain at the mm-wave band. The proposed design is the first antenna structure of its kind that employs a single DRA for dual-band operation with a high-frequency ratio. Using FFF 3D printing technology, the desired dielectric constant for different parts has been obtained by a low-loss filament and tuning the infill percentage. The achieved operation bandwidth (33% @ sub-6GHz and 27% @ mm-wave) and the efficiency (95% @ sub-6GHz and 80% @ mm-wave) are the highest in both bands compared to the previous works on dual-band antennas with high-frequency ratio as shown in Table 4. The radiation characteristics of the antenna are stable over both sub-6-GHz and mm-wave bands.

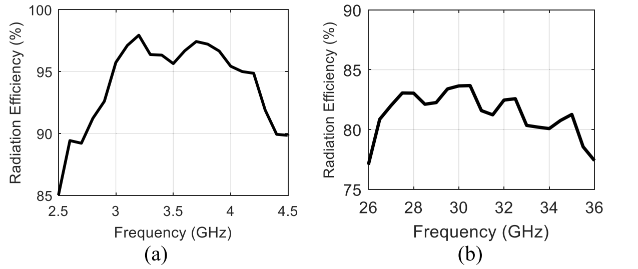

FIGURE 17. Measured radiation efficiency at (a) Sub-6-GHz and (b) mm-wave band.

REFERENCES

[1] J. Lan, Z. Yu, J. Zhou, and W. Hong, "An aperture-sharing array for (3.5, 28) GHz terminals with steerable beam in millimeter-wave band," *IEEE Trans. Antennas Propag.*, vol. 68, no. 5, pp. 4114–4119, May 2020.

[2] X.-H. Ding, W.-W. Yang, W. Qin, and J.-X. Chen, "A broadside shared aperture antenna for (3.5, 26) GHz mobile terminals with steerable beam in millimeter-waveband," *IEEE Trans. Antennas Propag.*, vol. 70, no. 3, pp. 1806–1815, Mar. 2022.

[3] M. M. S. Taheri, A. Abdipour, S. Zhang, and G. F. Pedersen, "Integrated millimeter-wave wideband end-fire 5G beam steerable array and low-frequency 4G LTE antenna in mobile terminals," *IEEE Trans. Veh. Technol.*, vol. 68, no. 4, pp. 4042–4046, Apr. 2019.

[4] Q. Liang, H. Aliakbari, and B. K. Lau, "Co-designed millimeter-wave and sub-6 GHz antenna for 5G smartphones," *IEEE Antennas Wireless Propag. Lett.*, vol. 21, pp. 1995–1999, 2022.

[5] R. S. Malfajani, F. B. Ashraf, and M. S. Sharawi, "A 5G enabled shared-aperture, dual-band, in-rim antenna system for wireless handsets," *IEEE Open J. Antennas Propag.*, vol. 3, pp. 1013–1024, 2022.

[6] Z.-X. Xia, K. W. Leung, N. Yang, and K. Lu, "Compact dual-frequency antenna array with large frequency ratio," *IEEE Trans. Antennas Propag.*, vol. 69, no. 4, pp. 2031–2040, Apr. 2021.

[7] W.-W. Yang, X.-H. Ding, T.-W. Chen, L. Guo, W. Qin, and J.-X. Chen, "A shared-aperture antenna for (3.5, 28) GHz terminals with end-fire and broadside steerable beams in millimeter wave band," *IEEE Trans. Antennas Propag.*, vol. 70, no. 10, pp. 9101–9111, Oct. 2022.

[8] W. M. Abdel-Wahab, D. Busuioc, and S. Safavi-Naeini, "Millimeter-wave high radiation efficiency planar waveguide series-fed dielectric resonator antenna (DRA) array: Analysis, design, and measurements," *IEEE Trans. Antennas Propag.*, vol. 59, no. 8, pp. 2834–2843, Aug. 2011.

[9] B. Zhang, Y.-X. Guo, H. Zirath, and Y. P. Zhang, "Investigation on 3-D-printing technologies for millimeter-wave and terahertz applications," *Proc. IEEE*, vol. 105, no. 4, pp. 723–736, Apr. 2017.

[10] F. Calignano et al., "Overview on additive manufacturing technologies," *Proc. IEEE*, vol. 105, no. 4, pp. 593–612, Apr. 2017.

[11] S. Alkaraki et al., "Compact and low-cost 3-D printed antennas metalized using spray-coating technology for 5G mm-wave communication systems," *IEEE Antennas Wireless Propag. Lett.*, vol. 17, pp. 2051–2055, 2018.

[12] G. Addamo et al., "3-D printing of high-performance feed horns from Ku- to V-bands," *IEEE Antennas Wireless Propag. Lett.*, vol. 17, pp. 2036–2040, 2018.

[13] M. Liang, C. Shemelya, E. MacDonald, R. Wicker, and H. Xin, "3-D printed microwave patch antenna via fused deposition method and ultrasonic wire mesh embedding technique," *IEEE Antennas Wireless Propag. Lett.*, vol. 14, pp. 1346–1349, 2015.

[14] J. Zhu, Y. Yang, D. Mcgloin, S. Liao, and Q. Xue, "3-D printed all-dielectric dual-band broadband reflectarray with a large frequency ratio," *IEEE Trans. Antennas Propag.*, vol. 69, no. 10, pp. 7035–7040, Oct. 2021.

[15] J. Huang, S. J. Chen, Z. Xue, W. Withayachumnankul, and C. Fumeaux, "Wideband endfire 3-D-printed dielectric antenna with designable permittivity," *IEEE Antennas Wireless Propag. Lett.*, vol. 17, pp. 2085–2089, 2018.

[16] J. Huang, S. J. Chen, Z. Xue, W. Withayachumnankul, and C. Fumeaux, "Impact of infill pattern on 3D printed dielectric resonator antennas," in *Proc. IEEE Asia–Pacific Conf. Antennas Propag. (APCAP)*, 2018, pp. 233–235.

[17] Z.-X. Xia, K. W. Leung, and K. Lu, "3-D-printed wideband multi-ring dielectric resonator antenna," *IEEE Antennas Wireless Propag. Lett.*, vol. 18, pp. 2110–2114, 2019.

[18] F. P. Chietera, R. Colella, and L. Catarinucci, "Dielectric resonators antennas potential unleashed by 3D printing technology: A practical application in the IoT framework," *Electronics*, vol. 11, no. 1, p. 64, 2022.

[19] P. Nayeri and G. Brennecka, "Wideband 3D-printed dielectric resonator antennas," in *Proc. IEEE Int. Symp. Antennas Propag. USNC/URSI Nat. Radio Sci. Meeting*, 2018, pp. 2081–2082.

[20] A. Goulas et al., "The impact of 3D printing process parameters on the dielectric properties of high permittivity composites," *Designs*, vol. 3, no. 4, p. 50, Nov. 2019.

[21] Z.-X. Xia, K. W. Leung, P. Gu, and R. Chen, "3-D-printed wideband high-efficiency dual-frequency antenna for vehicular communications," *IEEE Trans. Veh. Technol.*, vol. 71, no. 4, pp. 3457–3469, Apr. 2022.

[22] R. Sauleau, C. A. Fernandes, and J. R. Costa, "Review of lens antenna design and technologies for mm-wave shaped-beam applications," in *Proc. 11th Int. Symp. Antenna Technol. Appl. Electromagn.*, 2017, pp. 1–5.

[23] A. Artemenko, A. Mozharovskiy, A. Maltsev, R. Maslennikov, A. Sevastyanov, and V. Ssorin, "2D electronically beam steerable integrated lens antennas for mmWave applications," in *Proc. 42nd Eur. Microw. Conf.*, 2012, pp. 213–216.

[24] F. Meng and S. K. Sharma, "A wideband resonant cavity antenna with compact partially reflective surface," *IEEE Trans. Antennas Propag.*, vol. 68, no. 2, pp. 1155–1160, Feb. 2020.

[25] R. K. Mongia and P. Bhartia, "Dielectric resonator antennas—A review and general design relations for resonant frequency and bandwidth," *Int. J. Microw. Millimeter-Wave Comput.-Aided Eng.*, vol. 4, pp. 230–247, Jul. 1994.

[26] D. F. Filipovic, S. S. Gearhart, and G. M. Rebeiz, "Double-slot antennas on extended hemispherical and elliptical silicon dielectric lenses," *IEEE Trans. Microw. Theory Techn.*, vol. 41, no. 10, pp. 1738–1749, Oct. 1993.

[27] H. Frid, "Closed-form relation between the scan angle and feed position for extended hemispherical lenses based on ray tracing," *IEEE Antennas Wireless Propag. Lett.*, vol. 15, pp. 1963–1966, 2016.

[28] W. Xidong, G. V. Eleftheriades, and E. V. Deventer, "Design and characterization of single and multiple beam MM-wave circularly polarized substrate lens antennas for wireless communications," in *IEEE Antennas Propag. Soc. Int. Symp. Dig. Held Conjunction USNC/URSI Nat. Radio Sci. Meeting*, vol. 4, 1999, pp. 2408–2411.

[29] D. F. Filipovic, G. P. Gauthier, S. Raman, and G. M. Rebeiz, "Off-axis properties of silicon and quartz dielectric lens antennas," *IEEE Trans. Antennas Propag.*, vol. 45, no. 5, pp. 760–766, May 1997.

[30] A. H. Sihvola, *Electromagnetic Mixing Formulas and Applications*. London, U.K.: Inst. Electr. Eng., 1999.

[31] R. Simpkin, "Derivation of Lichtenecker's logarithmic mixture formula from Maxwell's equations," *IEEE Trans. Microw. Theory Techn.*, vol. 58, no. 3, pp. 545–550, Mar. 2010.

[32] B. Msallem, N. Sharma, S. Cao, F. S. Halbeisen, H.-F. Zeilhofer, and F. M. Thieringer, "Evaluation of the dimensional accuracy of 3D-printed anatomical mandibular models using FFF, SLA, SLS, MJ, and BJ printing technology," *J. Clin. Med.*, vol. 9, no. 3, p. 817, 2020.

REZA SHAMSAEE MALFAJANI (Graduate Student Member, IEEE) received the B.S. degree in electrical engineering from the University of Tehran, Tehran, Iran, in 2009, and the M.S. degree in electrical engineering from Tarbiat Modares University, Tehran, in 2012. He is currently pursuing the Ph.D. degree with Polytechnique Montréal, Montreal, QC, Canada, where he is also a member of the Poly-Grames Research Center. His research focuses on the periodic structures, antennas and RF, mm-wave, and terahertz designs. He received the Merit Scholarship Program for Foreign Students (PBEEE) in 2023, the Jocelyne and Jean C. Monty Doctoral Research Excellence Scholarship in 2022, and the Food Agility CRC Scholarship in 2021.

HAMED NIKNAM received the Ph.D. degree from McGill University, Montreal, QC, Canada, in 2020. He has been a member of the Research Center for High Performance Polymer and Composite Systems (CREPEC) since 2016. He is an FRQNT Award-Holder Postdoctoral Fellow with the Mechanical Engineering Department, Polytechnique Montreal. His previous research focused on 3-D printed architectured metamaterial for enhancing thermos-mechanical response of solid structures. Since 2020, he has been with the Laboratory for Multiscale Mechanics, Polytechnique Montreal. His current research is employing advanced additive manufacturing techniques for 5G applications.

SAMPADA BODKHE received the bachelor's degree in mechanical engineering from Visveswaraya Technological University, India, the master's degree in aerospace engineering from the Indian Institute of Technology Kanpur, India, and the Ph.D. degree from Polytechnique Montreal in 2017, where she developed piezoelectric inks and a technique to co-fabricate electrodes with piezoelectric sensors via co-extrusion-based 3-D direct-write technique. The research on the development of these self-powered sensors toward aero-elastic and biomedical applications was chosen as the 10 Best Discoveries of the Year 2018 by Quebec Science Magazine. She is an Assistant Professor with the Department of Mechanical Engineering, Polytechnique Montreal. As a visiting Ph.D. student with the Organic Robotics Laboratory, Cornell University, she worked on SLA-based 3-D printing of highly flexible actuators. After her Ph.D., she worked as a Postdoctoral Researcher with the Composite Materials and Adaptive Systems Laboratory, ETH Zurich, on establishing competencies in 3-D printing of adaptive systems, and multifunctional materials and structures. Prior to her Ph.D., she worked as an Edison Engineer with General Electric Aviation, India, on structural and thermal evaluation of components for LEAP 1B engines. She has keen interests in building an additive manufacturing platform for the fabrication of intelligent composite structures. She is currently also an Ambassador for the Montreal Chapter of Women in 3-D Printing and serves on the Advisory Board of Indian Women in 3-D Printing.

DANIEL THERRIAULT is a Full Professor with the Mechanical Engineering Department, Polytechnique Montreal. He currently holds the Safran-Polytechnique Industrial Chair on the additive manufacturing of reinforced polymers in 2018–2023 and formerly held a Canada Research Chair on the fabrication of advanced microsystems and materials in 2009–2019. He is the Co-Director of the Laboratory for Multiscale Mechanics, Polytechnique Montreal. His research interests are mainly related to additive manufacturing of advanced materials and multifunctional composites. His past contributions include the development of innovative additive manufacturing processes (e.g., freeform printing), the design and fabrication of nanocomposite materials for advanced aerospace applications, and the 3-D printing of carbon fiber-reinforced thermoplastic composites. Several important scientific contributions (∼120 refereed papers) in prestigious journals, such as *Nature Materials*, *Advanced Materials*, and *Additive Manufacturing*, and multiple innovations (ten patents) originated from the research activities of his research team. He worked or is working on many collaborative research projects with partners, such as Safran Group, Bombardier Aerospace, ArianeGroup, Bell Textron Canada, 3M, Dyze Design, NanoXplore, and the Canadian Space Agency.

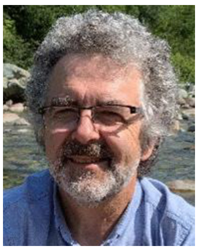

JEAN-JACQUES LAURIN (Senior Member, IEEE) received the B.Eng. degree in engineering physics from the Ecole Polytechnique de Montreal, Montreal, QC, Canada, in 1983, and the M.A.Sc. and Ph.D. degrees in electrical engineering from the University of Toronto, Toronto, ON, Canada, in 1986 and 1991, respectively. In 1991, he joined the Poly-Grames Research Centre, Ecole Polytechnique de Montreal, where he is currently a Professor. He is the Co-Director of STARaCom (Center for Systems, Technologies and Applications for Radiofrequency and Communications), a strategic research cluster in the province of Quebec. His research interests include antenna design and modeling, wave processing surfaces, near-field antenna measurement techniques, and electromagnetic compatibility.

MOHAMMAD S. SHARAWI (Senior Member, IEEE) is a Full Professor with the Electrical Engineering Department, University of Montréal (Polytechnique Montréal), Montreal, QC, Canada, where he is also a member of the Poly-Grames Research Center. He was with the King Fahd University of Petroleum and Minerals (KFUPM), Dhahran, Saudi Arabia, from 2009 to 2018. He founded and directed the Antennas and Microwave Structure Design Laboratory, KFUPM. He was a Visiting Professor with the Intelligent Radio Laboratory, Department of Electrical Engineering, University of Calgary, Calgary, AB, Canada, in Summer–Fall 2014. He was a Visiting Research Professor with Oakland University, Rochester, MI, USA, in Summer 2013. He has more than 350 papers published in refereed journals and international conferences, 11 book chapters (two of which in the Antenna Handbook, 5th edition, McGraw Hill, 2018), one single authored book titled *Printed MIMO Antenna Engineering* (Artech House, 2014), and the lead author of the recent book *Design and Applications of Active Integrated Antennas* (Artech House, 2018). He has 28 issued/granted and nine pending patents in the U.S. Patent Office. His research interests include multiband printed multiple-input–multiple-output (MIMO) antenna systems, reconfigurable and active integrated antennas, millimeter-wave MIMO antennas and integrated 4G/5G antennas, microwave sensors, applied electromagnetics, and computational methods. He was a recipient of the Abdul Hameed Shoman Foundation Award for Arab researchers for the category of wireless systems in 2020 in addition to various best IEEE conference paper awards. He is also serving as an Associate Editor for the IEEE ANTENNAS AND WIRELESS PROPAGATION LETTERS, *IET Microwaves, Antennas and Propagation*, and IEEE OPEN JOURNAL ON ANTENNAS AND PROPAGATION; and an Area Editor (Antennas and Microwave Devices and Systems) for *Microwave and Optical Technology Letters* (Wiley). He was the Specialty Chief Editor for the newly launched *Frontiers in Communications and Networks* journal for the System and Test-Bed design section. He has served on the technical and organizational program committees and organized several special sessions on MIMO antenna systems and architectures in several international conferences, such as EuCAP, APS, IMWS-5G, APCAP, and iWAT among many others for many years. He is also the IEEE Antennas and Propagation Society (APS) Chair of the Montreal section and an Active Member of the IEEE Member Benefits Committee leading the initiative of the APS Student Travel Grant. He is also the Regional Delegate of the EuRAAP in North America. He is a Distinguished Lecturer of APS in 2023–2025.